RSC Advances

PAPER

View Article Online
View Journal | View Issue

Cite this: *RSC Adv.*, 2018, **8**, 19353

Fe_3O_4 nanoclusters highly dispersed on a porous graphene support as an additive for improving the hydrogen storage properties of $LiBH_4$†

Guang Xu, ‡[a] Wei Zhang, ‡[b] Ying Zhang, *[a] Xiaoxia Zhao,[a] Ping Wen[a] and Di Ma[a]

Fe_3O_4 nanoclusters anchored on porous reduced graphene oxide (Fe_3O_4@rGO) have been synthesized by a one-step hydrothermal route, and then ball milled with $LiBH_4$ to prepare a hydrogen storage composite with a low onset dehydrogenation temperature, and improved dehydrogenation kinetics and rehydrogenation reversibility. The $LiBH_4$–20 wt% Fe_3O_4@rGO composite begins to release hydrogen at 74 °C, which is 250 °C lower than for ball-milled pure $LiBH_4$. Moreover, the composite can release 3.36 wt% hydrogen at 400 °C within 1000 s, which is 2.52 times as high as that of pure $LiBH_4$. Importantly, it can uptake 5.74 wt% hydrogen at 400 °C under 5 MPa H_2, and its hydrogen absorption capacity still reaches 3.73 wt% after 5 de/rehydrogenation cycles. The activation energy (E_a) of the hydrogen desorption of the composite is decreased by 79.78 kJ mol^{-1} when 20 wt% Fe_3O_4@rGO is introduced into $LiBH_4$ as a destabilizer and catalyst precursor, showing enhanced thermodynamic properties. It could be claimed that not only the destabilization of Fe_3O_4, but also the active Li_3BO_3 species formed *in situ*, as well as the wrapping effect of the graphene, synergistically improve the hydrogen storage properties of $LiBH_4$. This work provides insight into developing non-noble metals supported on functional graphene as additives to improve the hydrogen storage properties of $LiBH_4$.

Received 30th March 2018
Accepted 13th May 2018

DOI: 10.1039/c8ra02762e

rsc.li/rsc-advances

1. Introduction

Hydrogen is considered to be a promising energy carrier capable of solving global energy and environmental crises on account of its clean combustion and high energy density.[1] However, the major barrier for realizing its large-scale utilization is the shortage of safe hydrogen storage and transportation techniques.[2] Extensive efforts have been centered on developing safe and efficient solid hydrogen storage materials with high hydrogen density, low dehydrogenation temperature, and favorable reversibility.[3] Lithium borohydride ($LiBH_4$) has been regarded as one of the materials with the most potential in solid state hydrogen storage systems due to its high gravimetric hydrogen capacity (18.4 wt%).[4] However, it is too thermodynamically stable and kinetically slow at releasing hydrogen under moderate conditions, and high temperature and pressure are required for its rehydrogenation.[5] To overcome the poor thermodynamic and slow kinetic properties of $LiBH_4$, several strategies have been adopted to reduce its dehydrogenation temperature and improve its sorption rate, as well as its reversibility under benign conditions.[6]

One conventional strategy is doping with appropriate additives or catalysts, such as transition metals,[7,8] transition metal oxides[9], or halides,[10,11] which can effectively improve the hydrogen storage properties of $LiBH_4$. Among them, iron-based compounds have been found to be a class of additives with high catalytic activity. Yu *et al.*[12] investigated the effects of various oxides on the dehydrogenation behavior of $LiBH_4$, wherein Fe_2O_3 showed the best destabilization effect among the studied oxides (TiO_2, Nb_2O_5, Fe_2O_3, V_2O_5, and SiO_2). The $LiBH_4$–$2Fe_2O_3$ mixture started to release hydrogen below 100 °C, and 6 wt% hydrogen could be released after heating to 200 °C. Zhang *et al.*[13] found that the dehydrogenation temperature of $LiBH_4$ was significantly reduced by doping with small amounts of $FeCl_2$, and the complete hydrogen desorption of $LiBH_4$ could be achieved due to the formation of metal boride. Recently, a superior destabilization effect of $LiBH_4$ was realised through the addition of nano-sized nickel ferrite $NiFe_2O_4$, and the *in situ*-formed Fe_3O_4, NiB, and Fe_3B from the reaction between $LiBH_4$ and $NiFe_2O_4$ acted as the actual destabilization agents in accelerating the dehydrogenation properties of $LiBH_4$.[14] More recently, boron-based compounds like H_3BO_3,[15] HBO_2, and B_2O_3 [16] have been reported to effectively promote the

[a]*Department of Materials Science and Engineering, College of Science, China University of Petroleum (Beijing), Changping District, Beijing 102249, PR China. E-mail: Y.Zhang@cup.edu.cn; Fax: +86-010-89732273; Tel: +86-010-89732273*

[b]*Hebei Key Laboratory of Applied Chemistry, School of Environmental and Chemical Engineering, Yanshan University, Qinhuangdao 066004, PR China*

† Electronic supplementary information (ESI) available. See DOI: 10.1039/c8ra02762e

‡ These authors contributed equally to this work.

dehydrogenation of $LiBH_4$ due to the interactions between protonic and hydridic hydrogen. Cai *et al.*[17] found that nano-sized metal borides MB_x (M = Mg, Ti, Fe, and Si) played an important catalytic role in enhancing the hydrogen storage performance of $LiBH_4$, and the catalytic effects of MB_x were influenced largely by the Pauling electronegativity of M in MB_x and the interfacial contact character between $LiBH_4$ and MB_x.

Of particular interest is the fact that porous and nanostructured carbon materials as efficient catalysts or nanoscale frameworks can effectively lower the hydrogen evolution temperature and ameliorate the rehydrogenation conditions of $LiBH_4$.[18] In the case where $LiBH_4$ was ball milled with various carbons (graphite, single-walled carbon nanotubes, and activated carbon), all the carbon additives could improve the H-exchange kinetics and H-capacity of $LiBH_4$ due to heterogeneous nucleation and micro-confinement effects.[19] Besides this, other carbon hosts like activated carbon nanofibers,[20] fluorographite,[21] and nitrogen-doped hierarchically porous carbon[22] have also been used as substrates to destabilize or catalyze $LiBH_4$. Nevertheless, relying solely on this method still makes it difficult to achieve rapid reversible hydrogen absorption and desorption processes under mild conditions. Furthermore, nearly (or even more than) a 50 wt% capacity loss in the first dehydrogenation and rehydrogenation cycle was repeatedly observed in the carbon-added systems due to the addition of plenty of carbon materials to disperse or confine $LiBH_4$.[23,24]

Graphene has attracted great interest and has been applied in various areas, such as energy storage, sensors, and catalysis, on account of its unique characteristics.[25] The addition of functional graphene to $LiBH_4$ could result in a high hydrogen storage capacity, rapid kinetics, and excellent reversibility. Xu *et al.*[26,27] reported that precious metal (Pt and Pd) nanoparticles anchored onto graphene sheets could greatly improve the hydrogen desorption behavior and uptake reversibility of $LiBH_4$. The artful combination of catalysis and nanoconfinement has become a promising way to improve the dehydrogenation and rehydrogenation performance of $LiBH_4$. More recently, the hydrogen storage properties of $LiBH_4$ have been shown to be improved tremendously by ball milling with graphene-supported highly-dispersed nickel nanoparticles at a low addition amount.[28] Zhang *et al.*[29] reported that a remarkable improvement in the hydrogen sorption, thermodynamic, and kinetic performances of $LiBH_4$ could be realized by modification with three-dimensional porous fluorinated graphene.

Based on the previous studies, it is anticipated that Fe-based compounds can weaken the B–H bond and thus improve the hydrogen storage properties of $LiBH_4$. Fe_3O_4 has attracted considerable attention due to its low cost, eco-friendliness, and natural abundance, which are widely applicable in energy storage, environmental governance, and photocatalytic fields.[30,31] In this work, Fe_3O_4 nanoclusters assembled on porous reduced graphene oxide sheets (Fe_3O_4@rGO) have been prepared successfully by a facile one-step hydrothermal route, and then were characterized by scanning electron microscopy, transmission electron microscopy, X-ray diffraction, X-ray photoelectron spectroscopy, *etc.* Subsequently, the composite was employed as a destabilizer and catalytic additive for improving the dehydrogenation and rehydrogenation behavior of $LiBH_4$. The $LiBH_4$–20 wt% Fe_3O_4@rGO composite prepared by high-energy ball milling showed an enhanced hydrogen desorption performance and uptake reversibility compared with ball-milled pure $LiBH_4$. The catalytic effects of Fe_3O_4@rGO on the hydrogen storage properties of $LiBH_4$ were investigated and discussed in detail.

2. Experimental section

2.1 Materials

Commercially available $LiBH_4$ (95%, Aladdin), $FeCl_3 \cdot 6H_2O$ (AR, Aladdin), ascorbic acid (AR, Sinopharm Chemical Reagent Beijing Co., Ltd), $N_2H_4 \cdot H_2O$ (99%, Aladdin), and Fe_3O_4 (AR, Aladdin) were used as received, without further purification.

2.2 Synthesis of Fe_3O_4 nanoclusters supported on porous reduced graphene oxide sheets (Fe_3O_4@rGO)

The graphene oxide (GO) used in this work was prepared according to Hummer's method.[32] Fe_3O_4@rGO was synthesized on the basis of the reported procedure by Hu *et al.*[33] with a slight modification. Typically, 0.12 g GO was dispersed in 60 mL distilled water under ultrasound at room temperature, followed by slowly adding 0.90 g of $FeCl_3 \cdot 6H_2O$ and 1.76 g of ascorbic acid. Then, 10 mL $N_2H_4 \cdot H_2O$ was quickly added into the solution under vigorous stirring. Subsequently, the mixture was transferred to a 100 mL Teflon-lined autoclave and heated at 180 °C for 8 h. After filtration, washing, and freeze drying, the final product was designated as Fe_3O_4@rGO. For comparison, the reduced graphene oxide (rGO) was obtained by a simple hydrogen thermal reduction method. In brief, the GO was heated from room temperature to 500 °C under 1 MPa hydrogen with a heating rate of 5 °C min^{-1}, and held for 5 h in a home-made temperature programmed apparatus.

2.3 Preparation of the hydrogen storage composites

$LiBH_4$ was ball milled with the as-prepared Fe_3O_4@rGO nanohybrid with a mass ratio of 4 : 1 at 500 rpm for 10 h under an Ar atmosphere using a planetary Fritsch-P6 mill. The weight ratio of the ball to powder mixture was about 40 : 1. The ball-milling procedure was carried out by alternating 15 min of milling and 15 min of resting to avoid the temperature of the sample container rising. For comparison, pure $LiBH_4$ or the $LiBH_4$ composites with the addition of Fe_3O_4 and rGO were prepared following the same procedure. It should be pointed out that before the ball milling of Fe_3O_4@rGO, rGO, and Fe_3O_4 with $LiBH_4$, they were all dried at 120 °C for 12 h in a vacuum oven to remove any possible absorbed water on their surfaces, and were then stored in an Ar-filled glove box. The samples are hereafter labeled as $LiBH_4$, $LiBH_4$–Fe_3O_4, $LiBH_4$–rGO, and $LiBH_4$–Fe_3O_4@rGO. All the sample handling was performed in an Ar-filled glove box. The amounts of oxygen and water vapour inside the glove-box were kept below 1 ppm.

2.4 Characterization

The crystal structure and morphology of the samples were characterized by scanning electron microscopy (SEM, Hitachi

SU8010), transmission electron microscopy (TEM, Hitachi HT7700), X-ray diffraction (XRD, D/Max-2500/PC, Cu Kα radiation), and X-ray photoelectron spectrometry (XPS, Thermo Scientific K-Alpha+, Al Kα radiation). For the XRD studies, all the samples were smeared on a glass slide in the Ar-filled glove box, and then were covered by a layer of plastic film to avoid moisture and oxygen contact during measurement. This resulted in a scattering peak at $2\theta = 22°$ in the XRD pattern attributed to the plastic film coverage. The specific surface area and porosity of the Fe_3O_4@rGO nanohybrid were measured by nitrogen adsorption–desorption at 77 K using a Micromeritics TriStar II 3020 Analyzer. Fourier transform infrared (FTIR) spectra were obtained by a Nicolet 6700 FTIR spectrometer equipped with a MCT detector to record the features of the chemical bonding states of the samples. For the FTIR studies, the samples were milled with dry KBr with a mass ratio of 1 : 100 and pressed into one thin slice in the Ar-filled glove box, and then they were placed into a lab-built Ar-filled container to protect the samples from air and moisture during the transfer process. The thermodynamic analysis of the samples was carried out using a simultaneous thermal analyzer (DTG-60A) in air from room temperature to 900 °C, at a heating rate of 10 °C min^{-1}. Differential scanning calorimetry (DSC) measurements for the dehydrogenation of the samples were carried out using a Mettler Toledo TGA/DSC1 system at heating rates of 5, 10, 15, and 20 °C min^{-1} from 50 to 500 °C under an Ar flow (50 mL min^{-1}).

The hydrogen desorption and absorption properties were investigated using a Sievert-type apparatus manufactured by the General Research Institute for Nonferrous Metals. Temperature-programmed-desorption (TPD) experiments were carried out in a temperature range from room temperature to 620 °C, at a heating rate of 5 °C min^{-1}. The isothermal dehydrogenation and rehydrogenation measurements were performed at the desired temperature under initial hydrogen pressures of 0.01 MPa and 5 MPa, respectively. For the rehydrogenation measurement of the samples, the samples were first evacuated continuously until they did not release any more hydrogen, in order to make sure that they had completely released their hydrogen. Then, the isothermal rehydrogenation was performed at the desired temperature with an initial hydrogen pressure of 5 MPa for 1 h. In this work, the hydrogen contents of all the samples are presented based on the total weight of the composites, in order to make a comparison with the as-milled $LiBH_4$.

3. Results and discussion

3.1 Synthesis and characterization of as-prepared Fe_3O_4@rGO

The schematic synthesis procedure of the Fe_3O_4@rGO nanohybrid is illustrated in Scheme 1. Firstly, GO was sonicated in water to obtain nanosheets of a few layers, and the liquid was brown-yellow. Then, iron(III) chloride hexahydrate and ascorbic acid were added to the liquid under continuous stirring, so that the Fe^{3+} ions were thoroughly dispersed onto the GO surface by electrostatic interaction. Later, hydrazine hydrate was added dropwise into the liquid under vigorous stirring. After the liquid became dark, it was transferred into a Teflon-lined container and reacted at 180 °C for 8 h. Lastly, the black product was isolated, washed, and freeze-dried.

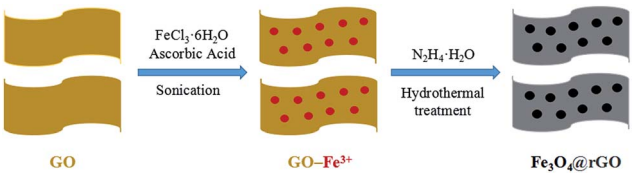

Scheme 1 Schematic illustration of the synthesis of the Fe_3O_4@rGO nanohybrid.

The microstructure of the as-prepared Fe_3O_4@rGO nanohybrid was studied using SEM and TEM. From the SEM image shown in Fig. 1a, it is clearly observed that tiny Fe_3O_4 nanoparticles are evenly distributed onto the surface of the large, disordered, and over-lapped graphene sheets. Fig. S1a† shows the typical morphology of GO, revealing the wrinkled sheet-like structure, and large, smooth surface. After the hydrogen thermal treatment, rGO with abundant wrinkles and defects is obtained (Fig. S1b†). Fig. 1b shows the TEM image of the Fe_3O_4@rGO nanohybrid, in which it can been found that the snowflake-like Fe_3O_4 nanoclusters consist of plentiful small particles of 5–6 nm in size, which are anchored uniformly onto the reduced graphene surface. The resultant Fe_3O_4@rGO nanohybrid is mainly composed of Fe, O, and C elements, according to the EDS analysis (Fig. S2†). N_2 adsorption–desorption isotherms and the corresponding pore size distribution curve of the nanohybrid are exhibited in Fig. 1c and d. Its specific surface area is calculated to be 119.3 m^2 g^{-1} based on the BET method. The pore volume is 0.374 cm^3 g^{-1}, with major pores located at about 3.7 nm and 14.7 nm in diameter, indicating the mesoporous characteristics of the as-prepared Fe_3O_4@rGO nanohybrid.

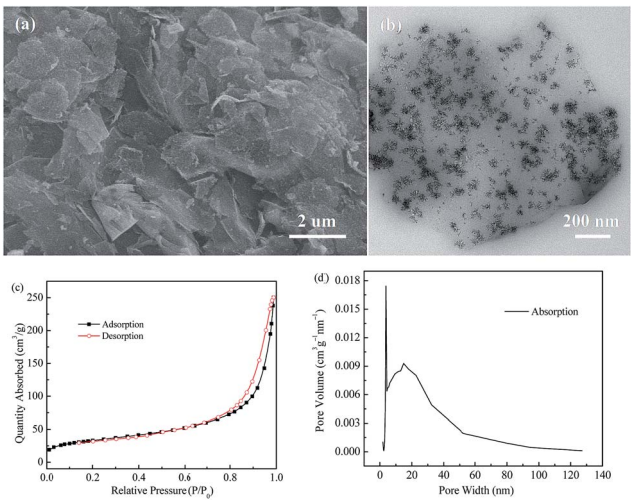

Fig. 1 (a) SEM image, (b) TEM image, (c) nitrogen adsorption–desorption isotherms, and (d) BJH pore-size distribution pattern of the as-prepared Fe_3O_4@rGO nanohybrid.

Fig. S3† shows the XRD patterns of the GO and rGO. For the GO, a well-defined peak is located at $2\theta = 10.8°$ with 0.87 nm *d*-spacing, indicating the presence of abundant oxygen-containing functional groups on the sides of the GO nanosheets.[34] However, the rGO has only a very low intensity peak around 25.8°, which indicates a distorted graphite structure and hence suggests the formation of rGO sheets.[35] The XRD pattern of the as-prepared Fe_3O_4@rGO nanohybrid is displayed in Fig. 2a. Some diffraction peaks occur at 30.1°, 35.6°, 43.1°, 57.0°, and 62.7°, which are in good agreement with the characteristic peaks of pure cubic Fe_3O_4 (JCPDF 65-3107). To further verify the surface chemical composition of Fe_3O_4@rGO, XPS analysis was carried out. Two typical characteristic peaks situated at the binding energies of 709.81 and 723.46 eV are attributed to the Fe $2p_{3/2}$ and Fe $2p_{1/2}$ of Fe_3O_4 (Fig. 2b).[36] The peak at 530.27 e V in the O 1s spectrum (Fig. 2c) can be assigned to the Fe–O bonds of Fe_3O_4@rGO.[37] TGA was used to quantify the loading amount of Fe_3O_4 in the Fe_3O_4@rGO nanohybrid, and was conducted from room temperature to 900 °C in air, at a heating rate of 10 °C min^{-1}. The TGA curves of Fe_3O_4@rGO and pure Fe_3O_4 are shown in Fig. 2d. There are two stages of weight loss for Fe_3O_4@rGO. The weight loss below 150 °C is ascribed to the evaporation of absorbed moisture. The abrupt weight loss from 192 °C to 425 °C is due to the burning of graphene in air. Based on the weight loss, 51.4 wt% graphene and 48.6 wt% Fe_3O_4 are estimated for the Fe_3O_4@rGO nanohybrid.

3.2 Hydrogen sorption, thermodynamic, and kinetic properties of the composites

It is well-known that the hydrogen storage properties of $LiBH_4$ can be altered by varying the amount of catalyst added. The preliminary experiments of $LiBH_4$ with different rGO addition amounts were performed and the results are shown in Fig. S4 and S5.† It can be seen that all the $LiBH_4$–*x* wt% rGO composites ($x = 11$, 20, and 33) exhibit improved dehydrogenation performances with respect to the ball-milled pure $LiBH_4$. The three composites have almost the same initial dehydrogenation temperature, being able to release hydrogen at 220.5 °C, but their final dehydrogenation capacity is different. With an increase in the addition amount, the final dehydrogenation capacity decreases gradually. Furthermore, the isothermal hydrogen desorption profiles at 400 °C of the as-milled $LiBH_4$ with and without the rGO composites are presented in Fig. S5.† The $LiBH_4$–20 wt% rGO composite exhibits the quickest hydrogen desorption rate among the $LiBH_4$-*x* wt% rGO composites, and it can release 3.46 wt% hydrogen after 3600 s, which is twice as large as the dehydrogenated capacity of ball-milled pure $LiBH_4$ under identical conditions. Taking the dehydrogenation temperature and kinetics into account, the addition of 20 wt% carbon materials is regarded as the best choice and $LiBH_4$–20 wt% y composites (y = Fe_3O_4, rGO, and Fe_3O_4@rGO) are prepared and further investigated in the later work.

Fig. 3 illustrates the TPD performances of ball-milled pure $LiBH_4$, $LiBH_4$–20 wt% Fe_3O_4, $LiBH_4$–20 wt% rGO, and $LiBH_4$–20 wt% Fe_3O_4@rGO composites from room temperature to 620 °C. The pure $LiBH_4$ starts to slowly release hydrogen at 324 °C. However, the $LiBH_4$–Fe_3O_4 and $LiBH_4$–rGO samples can release hydrogen at 78 °C and 220.5 °C, which are 246 °C and 103.5 °C lower than that of pure $LiBH_4$, respectively. The initial dehydrogenation temperature of the $LiBH_4$–20 wt% Fe_3O_4@rGO sample is as low as 74 °C, and a total dehydrogenation capacity of 8.88 wt% is obtained. It is also found that the $LiBH_4$–20 wt% Fe_3O_4 and $LiBH_4$–20 wt% Fe_3O_4@rGO samples showed quicker dehydrogenation rates than the pure $LiBH_4$ and $LiBH_4$–20 wt% rGO samples below 70 min, indicating that the destabilization effect of Fe_3O_4 is predominant. However, the $LiBH_4$–20 wt% Fe_3O_4@rGO and $LiBH_4$–20 wt% rGO samples showed quicker dehydrogenation rates than $LiBH_4$–20 wt% Fe_3O_4 and pure $LiBH_4$ after 70 min. The improvement of the dehydrogenation rate is attributed to the wrapping effect of the rGO and the catalytic effect of the *in situ*-formed Li_3BO_3. However, the formation of the stable species of Li_5FeO_4 in the $LiBH_4$–20 wt% Fe_3O_4@rGO composite may affect the dehydrogenation of

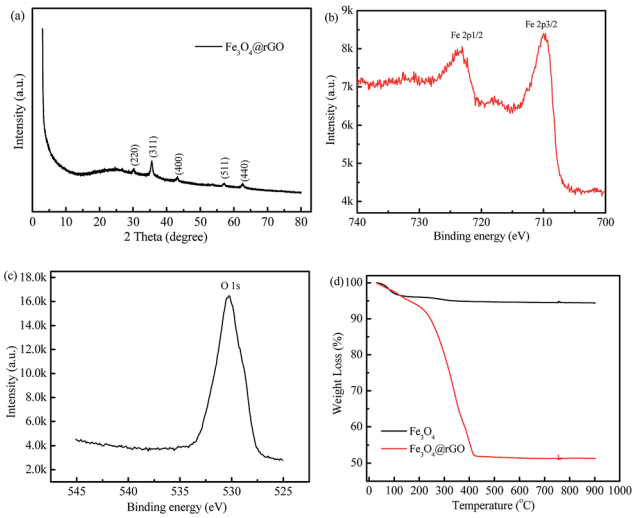

Fig. 2 (a) XRD pattern, (b) Fe 2p and (c) O 1s XPS spectra of the as-prepared Fe_3O_4@rGO nanohybrid, (d) TGA curves of Fe_3O_4@rGO and Fe_3O_4 in air ranging from room temperature to 900 °C.

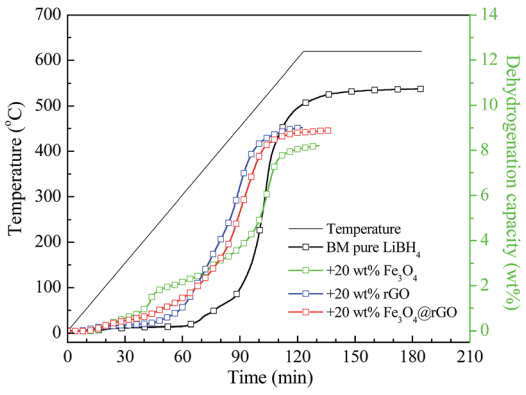

Fig. 3 TPD curves of ball-milled pure $LiBH_4$, $LiBH_4$–20 wt% Fe_3O_4, $LiBH_4$–20 wt% rGO, and $LiBH_4$–20 wt% Fe_3O_4@rGO composites.

$LiBH_4$, leading to the slightly reduced dehydrogenation performance when comparing it with the $LiBH_4$–20 wt% rGO composite. The significantly decreased initial dehydrogenation temperature and improved dehydrogenation rate of $LiBH_4$ indicate that the addition of Fe_3O_4@rGO by ball milling can clearly improve the desorption properties of $LiBH_4$.

To further study the desorption kinetics of the $LiBH_4$–20 wt% y composites (y = Fe_3O_4, rGO, and Fe_3O_4@rGO), DSC tests at different heating rates were performed to evaluate the activation energy (E_a) of these composites using Kissinger's method:[38]

$$\frac{d\left[\ln\left(\frac{\beta}{T_m^2}\right)\right]}{d\left[\frac{1}{T_m}\right]} = -\frac{E_a}{R}$$

in which β is the heating rate, T_m is the peak temperature, and R is the ideal gas constant. In this work, T_m is calculated using the DSC results obtained under the diverse heating rates of 5, 10, 15, and 20 °C min^{-1}. The DSC curves of the $LiBH_4$–20 wt% Fe_3O_4@rGO composite are shown in Fig. 4a. Fig. S6† presents the DSC curves of the $LiBH_4$–20 wt% Fe_3O_4 and $LiBH_4$–20 wt% rGO composites. The dependence of $\ln(\beta/T_m)$ *vs.* $1/T_m$ of the composites is shown in Fig. 4b. The value of E_a is calculated to be 102.02 kJ mol^{-1} for the $LiBH_4$–Fe_3O_4@rGO composite, which is much smaller than that of ball-milled pure $LiBH_4$ (181.80 kJ mol^{-1}).[39] This suggests that the E_a is significantly affected when using Fe_3O_4@rGO as a destabilizer and catalytic additive, which effectively decreases the energy barrier of $LiBH_4$ in the dehydrogenation process and thus causes the rapid dehydrogenation behavior of the composite.

Isothermal dehydrogenation measurements were carried out to explore the effect of Fe_3O_4@rGO on the dehydrogenation kinetics of $LiBH_4$. Fig. 5a shows the isothermal dehydrogenation curves of the $LiBH_4$–20 wt% y composites (y = Fe_3O_4, rGO, and Fe_3O_4@rGO) at 400 °C, under an initial hydrogen pressure of 0.01 MPa. The $LiBH_4$–20 wt% Fe_3O_4@rGO sample shows a faster hydrogen desorption rate than the other three hydrogen storage materials, and it can release 3.84 wt% hydrogen within 3600 s, whereas the pure $LiBH_4$, $LiBH_4$–20 wt% Fe_3O_4, and $LiBH_4$–20 wt% rGO samples can release 1.71, 2.04, and 3.47 wt% hydrogen under the same conditions, respectively. In addition, the dehydrogenation curves of the $LiBH_4$–20 wt% Fe_3O_4@rGO composite at different temperatures are shown in Fig. 5b. The composite is capable of releasing 2.28, 3.84, and 5.93 wt% hydrogen at 350, 400, and 450 °C, respectively. Remarkably, Fe_3O_4@rGO has a superior catalytic effect on the dehydrogenation kinetics and capacity of $LiBH_4$ compared with Fe_3O_4 or rGO alone. The improvement in the hydrogen storage performance not only comes from the destabilization of the Fe_3O_4 NPs, but also from the confinement of the rGO.[18,40] It is speculated that their synergistic effects will assist in improving the dehydrogenation performance of $LiBH_4$. The newly formed structural defects and the close contact between the

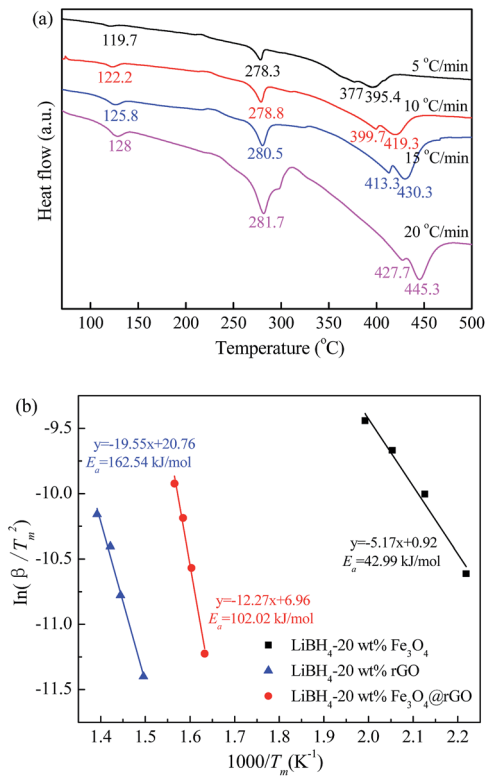

Fig. 4 (a) DSC curves for the $LiBH_4$–20 wt% Fe_3O_4@rGO composite at various heating rates and (b) Kissinger's plots of E_a for the $LiBH_4$–20 wt% y composites (y = Fe_3O_4, rGO, and Fe_3O_4@rGO).

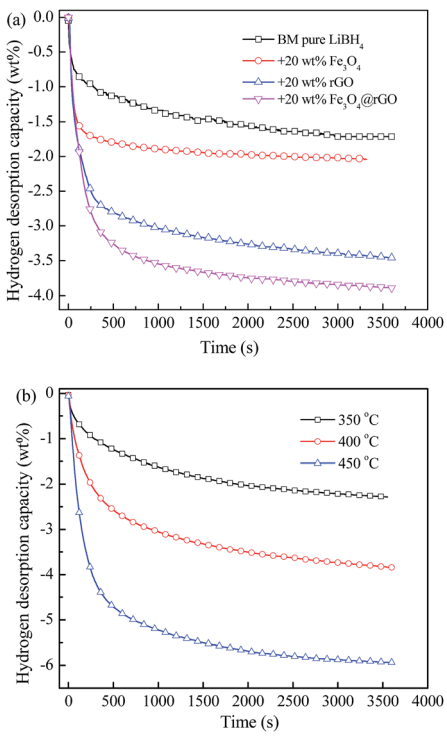

Fig. 5 Isothermal dehydrogenation curves of ball-milled (a) pure $LiBH_4$ and $LiBH_4$–20 wt% y composites (y = Fe_3O_4, rGO, and Fe_3O_4@rGO) at 400 °C, and (b) the $LiBH_4$–20 wt% Fe_3O_4@rGO composite at different temperatures.

Fe_3O_4@rGO and $LiBH_4$ during the ball milling process will also help achieve an enhanced dehydrogenation performance of $LiBH_4$.

Fig. 6a demonstrates the isothermal rehydrogenation curves at 400 °C for ball-milled pure $LiBH_4$ and the $LiBH_4$ composites with 20 wt% Fe_3O_4, rGO, and Fe_3O_4@rGO, under an initial hydrogen pressure of 5 MPa. The $LiBH_4$–20 wt% Fe_3O_4@rGO composite can absorb 5.45 wt% hydrogen within 3600 s. However, the pure $LiBH_4$, $LiBH_4$–20 wt% Fe_3O_4, and $LiBH_4$–20 wt% rGO composites can only absorb 2.36, 4.18, and 4.86 wt% hydrogen under the same conditions, respectively. Therefore, it is concluded that adding Fe_3O_4@rGO into $LiBH_4$ can result in a higher hydrogen storage capacity and quicker ab/desorption kinetics. In order to study the reversible hydrogen storage performance, the $LiBH_4$–20 wt% Fe_3O_4@rGO composite is rehydrogenated at 400 °C under 5 MPa H_2 for 1 h after its complete dehydrogenation, and the cyclic rehydrogenation curves are shown in Fig. 6b. The composite exhibits superior rehydrogenation behavior and an absorption capacity of 3.73 wt% after 5 cycles of hydrogen de/absorption is achieved, which is up to 69.1% of the initial hydrogen absorption capacity for the composite. However, pure $LiBH_4$ requires extremely harsh conditions of 600 °C and 35 MPa hydrogen pressure to rehydrogenate.[41] Obviously, the $LiBH_4$–Fe_3O_4@rGO composite shows a higher hydrogen absorption capacity than the composites with Fe_3O_4 or rGO. Thus, Fe_3O_4@rGO can simultaneously ameliorate the hydrogen release and uptake reversibility for the $LiBH_4$ system under moderate conditions, which is largely attributed to the combined effects of the reduced graphene oxide and Fe_3O_4 NPs.

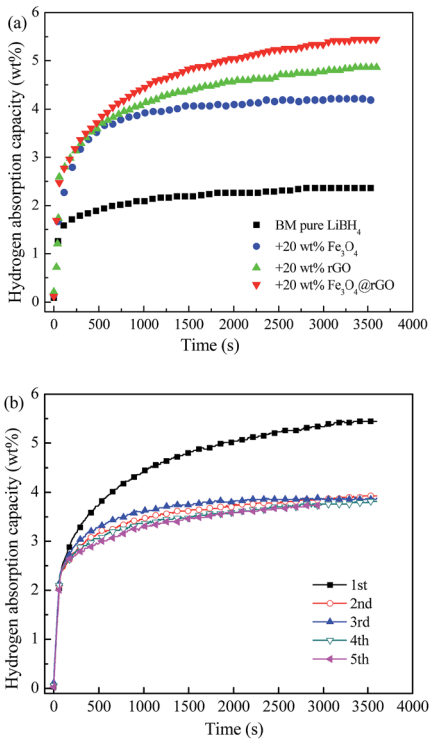

Fig. 6 (a) Isothermal rehydrogenation curves of the pure $LiBH_4$ and $LiBH_4$–20 wt% y composites (y = Fe_3O_4, rGO, and Fe_3O_4@rGO), and (b) the rehydrogenation cycling stability of the $LiBH_4$–20 wt% Fe_3O_4@rGO composite at 400 °C under 5 MPa H_2.

3.3 Discussion and deduction of the reaction mechanism

To investigate the effect of morphology on the improvement of the hydrogen storage properties of the $LiBH_4$–20 wt% Fe_3O_4@rGO composite, microstructural analysis of the composite was performed using SEM techniques. Fig. 7a shows that the composite has many defects and pores on its surface, with some particles, in the range of several tens of nanometers to several microns, encapsulated by graphene sheets. A high resolution SEM image is shown in Fig. S7† to further demonstrate the pores and particles of the as-milled $LiBH_4$–20 wt% Fe_3O_4@rGO sample. It can be observed that many small particles are wrapped tightly by the rGO sheets. After dehydrogenation at 400 °C (Fig. 7b), numerous wrinkles and channels randomly scattered on the sample surface appear. Furthermore, the dehydrogenated sample is still wrapped tightly by the rGO sheets. It is speculated that Fe_3O_4@rGO might play the role of a heterogeneous nucleation site for the $LiBH_4$ decomposition by providing more hydrogen diffusion pathways and it may also prevent agglomeration during the dehydrogenation process. The uniform dispersion and smaller particle size will benefit the hydrogen desorption and absorption behavior of $LiBH_4$.[42]

In order to further analyze the effect of Fe_3O_4@rGO on the hydrogen storage properties of $LiBH_4$, the $LiBH_4$–20 wt% Fe_3O_4@rGO composite in different states was assessed using XRD and FTIR techniques. In order to investigate the effects of rGO and Fe_3O_4 on $LiBH_4$ individually, XRD patterns of the $LiBH_4$–20 wt% rGO and $LiBH_4$–20 wt% Fe_3O_4 composites were also obtained (Fig. S7 and S8†). As shown in Fig. S8a,† the intense characteristic peaks of $LiBH_4$ can be clearly seen after ball milling, and the $LiBO_2$ phase is formed due to the reaction between $LiBH_4$ and the O in the rGO. After it dehydrogenates at 400 °C (Fig. S8b†), $LiBH_4$ can completely decompose, the $LiBO_2$ converts to Li_3BO_3, and the Li_3BO_3 exists in the later hydrogenation process (Fig. S8c†). As for the ball-milled $LiBH_4$–20 wt% Fe_3O_4 composite (Fig. S9a†), apart from the characteristic peaks of $LiBH_4$ and Fe_3O_4, $LiBO_2$ and Li_5FeO_4 peaks are also detected. For its dehydrogenated sample (Fig. S9b†), Li_5FeO_4 still exists. $LiBH_4$, Fe_3O_4, and $LiBO_2$ disappear, while LiH and Li_3BO_3 phases appear, which indicates there are some reactions between $LiBH_4$ and Fe_3O_4 during the dehydrogenation reaction. Similar results are observed for the $LiBH_4$–20 wt% Fe_3O_4@rGO

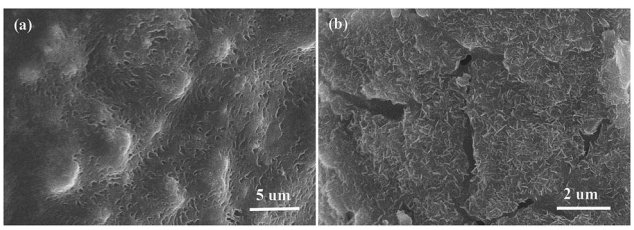

Fig. 7 SEM images of the $LiBH_4$–20 wt% Fe_3O_4@rGO composite: (a) as-milled and (b) after desorption at 400 °C.

composite (Fig. 8a and b). The characteristic peaks of the $LiBH_4$, Fe_3O_4, $LiBO_2$, and Li_5FeO_4 species are verified for the ball-milled $LiBH_4$–Fe_3O_4@rGO sample, confirming that $LiBH_4$ can react with Fe_3O_4 during the ball milling process. It is believed that Fe_3O_4 can react with $LiBH_4$ to form $LiBO_2$ and Li_5FeO_4. After dehydrogenation at 400 °C, the formed $LiBO_2$ can react further with the remaining $LiBH_4$ to generate Li_3BO_3.[43] The Li_3BO_3 and Li_5FeO_4 still exist in the hydrogenation reaction (Fig. 8c), wherein Li_3BO_3 acts as the actual active species for improving the reversible hydrogen storage properties of $LiBH_4$.[44] However, the formation of thermodynamically stable compounds like Li_3BO_3 and Li_5FeO_4 is an important reason for the reduced rehydrogenation capacity. The possible hydrogen desorption reactions of the $LiBH_4$–20 wt% Fe_3O_4@rGO composite may be expressed as follows:

$$7LiBH_4 + 2Fe_3O_4 \rightarrow 2LiBO_2 + Li_5FeO_4 + 5FeB + 14H_2$$

$$2LiBH_4 \rightarrow 2LiH + 2B + 3H_2$$

$$3LiBH_4 + 3LiBO_2 \rightarrow 2Li_3BO_3 + 4B + 6H_2$$

Although $LiBH_4$ can reform in the rehydrogenation reaction, the existence of LiH in this state indicates that the rehydrogenation reaction is incomplete, which may be another reason for the degradation of the cyclic hydrogen absorption capacity of the $LiBH_4$–Fe_3O_4@rGO composite.

To further prove that $LiBH_4$ is generated again after rehydrogenation, FTIR analysis of the as-milled, dehydrogenated, and rehydrogenated $LiBH_4$–20 wt% Fe_3O_4@rGO samples was carried out. From Fig. 9a, characteristic peaks of B–H stretching bands at 2227, 2292, and 2387 cm^{-1} and B–H bending bands at 1127 cm^{-1} are revealed. For the dehydrogenated sample (Fig. 9b), these characteristic bands of B–H are absent, indicating the complete decomposition of $LiBH_4$ in the hydrogen desorption process. In contrast, the characteristic peaks of the B–H bands are visible in the spectrum of the rehydrogenated sample (Fig. 9c). The disappearance and re-emergence of the B–H bands are strong evidence for the reversibility of the

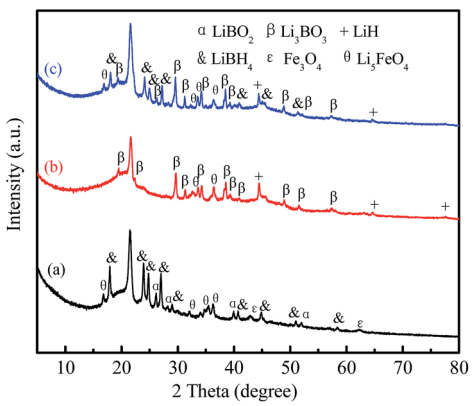

Fig. 8 XRD patterns of the $LiBH_4$–20 wt% Fe_3O_4@rGO composite: (a) as-milled, (b) after desorption at 400 °C, and (c) after absorption at 400 °C.

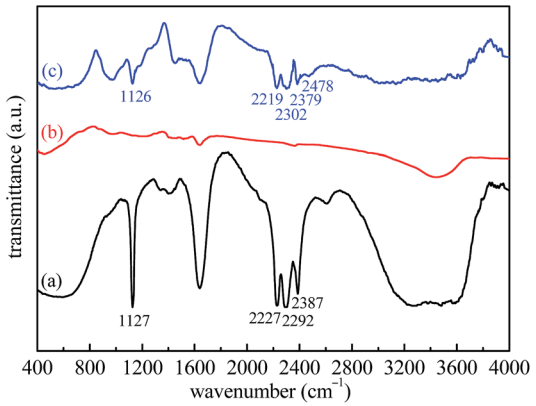

Fig. 9 FTIR spectra of the $LiBH_4$–20 wt% Fe_3O_4@rGO composite: (a) as-milled, (b) after desorption at 400 °C, and (c) after absorption at 400 °C.

hydrogen desorption/absorption reactions. However, we also observe a new absorption peak at 2478 cm^{-1}, which can be assigned to $Li_2B_{12}H_{12}$.[45] Although $Li_2B_{12}H_{12}$ can react with LiH to generate $LiBH_4$, this reaction requires harsh conditions of 500 °C and 100 MPa H_2 for 72 h.[46,47] In our work, the rehydrogenation was carried out under the moderate conditions of 400 °C and 5 MPa H_2 for 1 h. Therefore, some $Li_2B_{12}H_{12}$ and LiH still remained in the rehydrogenated state for the $LiBH_4$–20 wt% Fe_3O_4@rGO sample, suggesting that the reaction between $Li_2B_{12}H_{12}$ and LiH was not complete, thus affecting its cyclic rehydrogenation behavior. Furthermore, FTIR spectra of the $LiBH_4$–20 wt% rGO composite in different states were also obtained and are shown in Fig. S10.† The $LiBH_4$ can decompose and regenerate likewise after the dehydrogenation and rehydrogenation of the $LiBH_4$–20 wt% rGO composite (Fig. S10b and c†). The peak of $Li_2B_{12}H_{12}$ at 2477 cm^{-1} is also detected in the rehydrogenated $LiBH_4$–rGO sample. The surface morphology of the $LiBH_4$–20 wt% Fe_3O_4@rGO composite after the first hydrogenation changed greatly, as shown in Fig. S11.† Although the rehydrogenated sample is still wrapped tightly by the rGO nanosheets, the amount of wrinkles and channels on its surface apparently decreases. The morphology change can be another reason for the degradation of the cyclic hydrogen absorption capacity of the $LiBH_4$–20 wt% Fe_3O_4@rGO composite, but its rehydrogenation performance is still superior to that of pure $LiBH_4$.

Based on the above analyses, we conclude that some $LiBH_4$ can be confined in the pores of the reduced graphene oxide sheets, while the remaining $LiBH_4$ spreads evenly over the surface after ball milling due to the loose porous structure of the sheets. Fe_3O_4@rGO acts as a destabilization agent by reacting with $LiBH_4$ to decrease its onset dehydrogenation temperature. The *in situ*-formed active Li_3BO_3 species during the dehydrogenation process has an actual catalytic effect on improving the dehydrogenation kinetics and rehydrogenation reversibility of $LiBH_4$. Simultaneously, abundant structural defects and channels are created during this process. The wrapping effect of the rGO nanosheets is proven to be able to effectively prevent the

nucleated particles from agglomerating during the dehydrogenation and rehydrogenation cycles.[48] In this regard, the destabilization, catalysis, and wrapping effect of the Fe_3O_4@rGO nanohybrid contribute jointly to the improved hydrogen storage performance of $LiBH_4$.

4. Conclusions

In this study, porous reduced graphene oxide sheets decorated with Fe_3O_4 nanoclusters were synthesized by a facile hydrothermal method. The Fe_3O_4@rGO nanohybrid, serving as a destabilizer and catalyst precursor, is added to $LiBH_4$, resulting in the improvement of its hydrogen storage properties. The onset dehydrogenation temperature is reduced to 74 °C for the $LiBH_4$–20 wt% Fe_3O_4@rGO composite, which is 250 °C lower than that of ball-milled pure $LiBH_4$. Rehydrogenation with a promoted cycling stability is achieved at 400 °C under 5 MPa H_2. The addition of Fe_3O_4@rGO also decreases the E_a of the dehydrogenation reaction of $LiBH_4$ to 102.02 kJ mol^{-1}, suggesting excellent desorption kinetics, and it can release 3.89 wt% hydrogen at 400 °C after 3600 s, which is 2.27 times as high as pure $LiBH_4$. The significantly enhanced hydrogen storage properties of the composite are not only attributed to the destabilization derived from Fe_3O_4, but also the *in situ*-formed active Li_3BO_3 species in the decomposition process, as well as the wrapping of the rGO sheets. This work may provide insight into new applications of Fe_3O_4@rGO and the addition of other functional graphenes decorated with non-noble metals into $LiBH_4$, in order to fabricate hydrogen storage materials of desirable performance.

Conflicts of interest

The authors declare no competing financial interest.

Acknowledgements

This work was financially supported by the National Natural Science Foundation of China (51571173, 216762896 and U1162118), the Specialized Research Fund for the Doctoral Program of Higher Education of China (20130007110008), and the Beijing Young Talents Plan (YEPT0687).

References

1 X. B. Yu, Z. W. Tang, D. L. Sun, L. Z. Ouyang and M. Zhu, *Prog. Mater. Sci.*, 2017, **88**, 1–48.
2 R. Chamoun, U. B. Demirci and M. Philippe, *Energy Technol.*, 2015, **3**, 100–117.
3 H. Wang, H. J. Lin, W. T. Cai, L. Z. Ouyang and M. Zhu, *J. Alloys Compd.*, 2016, **658**, 280–300.
4 Y. Wu, X. J. Jiang, J. Chen, Y. Qi, Y. X. Zhang, H. Fu, J. Zheng and X. G. Li, *Dalton Trans.*, 2017, **46**, 4499–4503.
5 H. Q. Liu, L. F. Jiao, Y. P. Zhao, K. Z. Cao, Y. C. Liu, Y. J. Wang and H. T. Yuan, *J. Mater. Chem. A*, 2014, **2**, 9244–9250.
6 J. W. Huang, Y. R. Yan, L. Z. Ouyang, H. Wang, J. W. Liu and M. Zhu, *Dalton Trans.*, 2014, **43**, 410–413.
7 P. Ngene, M. R. V. Zwienen and P. E. D. Jongh, *Chem. Commun.*, 2010, **46**, 8201–8820.
8 M. Meggouh, D. M. Grant and G. S. Walker, *J. Phys. Chem. C*, 2011, **115**, 22054–22061.
9 X. L. Si, F. Li, L. X. Sun, F. Xu, S. S. Liu, J. Zhang, M. Zhu, L. Z. Ouyang and D. L. Sun, *J. Phys. Chem. C*, 2011, **19**, 9780–9786.
10 F. Fang, Y. T. Li, Y. Song, D. L. Sun, Q. G. Zhang, L. Z. Ouyang and M. Zhu, *J. Phys. Chem. C*, 2011, **115**, 13528–13533.
11 W. T. Cai, H. Wang, L. F. Jiao, Y. J. Wang and M. Zhu, *Int. J. Hydrogen Energy*, 2013, **38**, 3304–3312.
12 X. B. Yu, D. M. Grant and G. S. Walker, *J. Phys. Chem. C*, 2009, **113**, 17945–17949.
13 B. J. Zhang and B. H. Liu, *Int. J. Hydrogen Energy*, 2010, **35**, 7288–7294.
14 J. Zhang, P. Li, Q. Wan, F. Q. Zhai, A. A. Volinsky and X. H. Qu, *RSC Adv.*, 2015, **5**, 81212–81219.
15 Y. Wu, X. J. Jiang, J. Chen, Y. Qi, Y. X. Zhang, H. Fu, J. Zheng and X. G. Li, *Dalton Trans.*, 2017, **46**, 4499–4503.
16 W. T. Cai, J. Chen, L. Y. Liu, Y. Z. Yang and H. Wang, *J. Mater. Chem. A*, 2017, **6**, 1171–1180.
17 W. T. Cai, Y. Z. Yang, P. J. Tao, L. Z. Ouyang and H. Wang, *Dalton Trans.*, 2018, **47**, 4987–4993.
18 J. Xu, R. R. Meng, J. Y. Cao, X. F. Gu, Z. Q. Qi, W. C. Wang and Z. D. Chen, *Int. J. Hydrogen Energy*, 2013, **38**, 2796–2803.
19 Z. Z. Fang, X. D. Kang and P. Wang, *Int. J. Hydrogen Energy*, 2010, **35**, 8247–8252.
20 S. Thiangviriya and R. Utke, *Int. J. Hydrogen Energy*, 2015, **40**, 4167–4174.
21 L. T. Zhang, L. X. Chen, X. Z. Xiao, Z. W. Chen, S. K. Wang, X. L. Fan, S. Q. Li, H. W. Ge and Q. D. Wang, *Int. J. Hydrogen Energy*, 2014, **39**, 896–904.
22 Y. Zhao, Y. C. Liu, H. Y. Kang, K. Z. Cao, Y. J. Wang and L. F. Jiao, *Int. J. Hydrogen Energy*, 2016, **41**, 17175–17182.
23 P. A. Ward, J. A. Teprovich Jr, B. Peters, J. Wheeler, R. N. Compton and R. R. Zidan, *J. Phys. Chem. C*, 2013, **117**, 22569–22575.
24 K. K. Wang, X. D. Kang, J. W. Ren and P. Wang, *J. Alloys Compd.*, 2016, **685**, 242–247.
25 Y. W. Zhu, S. Murali, W. W. Cai, X. S. Li, J. W. Suk, J. R. Potts and R. S. Ruoff, *Adv. Mater.*, 2010, **22**, 3906–3924.
26 J. Xu, Z. Q. Qi, J. Y. Cao, R. R. Meng, X. F. Gu, W. C. Wang and Z. D. Chen, *Dalton Trans.*, 2013, **42**, 12926–12933.
27 J. Xu, R. R. Meng, J. Y. Cao, X. F. Gu, W. L. Song, Z. Q. Qi, W. C. Wang and Z. D. Chen, *J. Alloys Compd.*, 2013, **564**, 84–90.
28 J. Xu, Y. Li, J. Y. Cao, R. R. Meng, W. C. Wang and Z. D. Chen, *Catal. Sci. Technol.*, 2015, **5**, 1821–1828.
29 W. Zhang, G. Xu, L. J. Chen, S. Y. Pan, X. Jing, J. S. Wang and S. M. Han, *Int. J. Hydrogen Energy*, 2017, **42**, 15262–15270.
30 G. M. Zhou, D. W. Wang, F. Li, L. L. Zhang, N. Li, Z. S. Wu, L. Wen, G. Q. Lu and H. M. Cheng, *Chem. Mater.*, 2010, **22**, 5306–5313.
31 B. P. Lu, Z. Zhang, J. H. Hao and J. L. Tang, *RSC Adv.*, 2014, **4**, 21909–21917.
32 W. S. Hummers and R. E. Offeman, *J. Am. Chem. Soc.*, 1958, **80**, 1339.

33 J. Su, M. H. Cao, L. Ren and C. W. Hu, *J. Phys. Chem. C*, 2011, **115**, 14469–14477.
34 J. Z. Wang, G. H. Zhao, L. Y. Jing, X. M. Peng and Y. F. Li, *Biochem. Eng. J.*, 2015, **98**, 75–83.
35 A. K. Mishra and S. Ramaprabhu, *J. Appl. Phys.*, 2014, **116**, 064306.
36 L. H. Zhuo, Y. Q. Wu, L. Y. Wang, J. Ming, Y. C. Yu, X. B. Zhang and F. Y. Zhao, *J. Mater. Chem. A*, 2013, **1**, 3954–3960.
37 R. Kumar, R. K. Singh, A. R. Vaz, R. Savu and S. A. Moshkalev, *ACS Appl. Mater. Interfaces*, 2017, **9**, 8880–8890.
38 G. P. Tu, X. Z. Xiao, T. Qin, Y. Q. Jiang, S. Q. Li, H. W. Ge and L. X. Chen, *RSC Adv.*, 2015, **5**, 51110–51115.
39 J. S. Wang, Z. B. Wang, Y. Li, D. D. Ke, X. Z. Lin, S. M. Han and M. Z. Ma, *Int. J. Hydrogen Energy*, 2016, **41**, 13156–13162.
40 A. Gasnier and F. C. Gennari, *RSC Adv.*, 2017, **7**, 27905–27912.
41 W. T. Cai, H. Wang, J. W. Liu, L. F. Jiao, Y. J. Wang, L. Z. Ouyang, T. Sun, D. L. Sun, H. H. Wang, X. D. Yao and M. Zhu, *Nano Energy*, 2014, **10**, 235–244.
42 J. Shao, X. Z. Xiao, X. L. Fan, L. T. Zhang, S. Q. Li, H. W. Ge, Q. D. Wang and L. X. Chen, *J. Phys. Chem. C*, 2014, **118**, 11252–11260.
43 L. L. Guo, Y. Li, Y. F. Ma, Y. Liu, D. D. Peng, L. Zhang and S. M. Han, *Int. J. Hydrogen Energy*, 2016, **42**, 2215–2222.
44 Y. F. Ma, Y. Li, T. Liu, X. Zhao, L. Zhang, S. M. Han and Y. J. Wang, *J. Alloys Compd.*, 2016, **689**, 187–191.
45 M. P. Pitt, M. Paskevicius, D. H. Brown, D. A. Sheppard and C. E. Buckley, *J. Am. Chem. Soc.*, 2013, **135**, 6930–6941.
46 Y. G. Yan, H. Wang, M. Zhu, W. T. Cai, D. Rentsch and A. Remhof, *Crystals*, 2018, **8**, 131–138.
47 J. L. White, R. J. Newhouse, J. Z. Zhang, T. J. Udovic and V. Stavila, *J. Phys. Chem. C*, 2016, **120**, 25725–25731.
48 Y. Y. Zhu, J. X. Zou and X. Q. Zeng, *RSC Adv.*, 2015, **5**, 82916–82923.